

## SPECIAL ISSUE ARTICLE

# Preparation of concrete specimen for internal sulfate attack analysis using electron backscatter diffraction

 R. Sharon Uwanyuze<sup>1</sup> | Lucas Enright<sup>1</sup> | Ji Yao Zhang<sup>2</sup> | Stefan Schafföner<sup>1,2,3</sup> 

<sup>1</sup> Department of Materials Science and Engineering, University of Connecticut, Storrs, Connecticut, USA

<sup>2</sup> Institute of Materials Science, University of Connecticut, Storrs, Connecticut, USA

<sup>3</sup> Chair of Ceramic Materials Engineering, University of Bayreuth, Bayreuth 95447, Germany

## Correspondence

Stefan Schafföner, Chair of Ceramic Materials Engineering, University of Bayreuth, Bayreuth 95447, Germany.

Email:

[stefan.schaffoener@uni-bayreuth.de](mailto:stefan.schaffoener@uni-bayreuth.de)

## Funding information

University of Connecticut

## Abstract

Concrete cores were obtained from houses in eastern Connecticut, USA, that had varying degrees of crumbling foundations and wall cracking. Electron backscatter diffraction (EBSD) was used simultaneously with energy dispersive X-ray spectroscopy to investigate the degradation of these samples. This combination allowed the precise correlation of elemental composition with mineral crystallography phase mapping. EBSD examination showed the presence of pyrrhotite, pyrite, and marcasite phases in some of the samples, whereas internal sulfate attack (ISA) is triggered by the release of sulfates through the oxidation of such iron sulfides. Secondary expansion products from ISA are associated with foundation cracking, wall bulging, and drastically decreased structural stability. The main contribution of this study is therefore an automated procedure for preparation of concrete samples and analysis of aggregates using EBSD.

## KEYWORDS

degradation, electron backscatter diffraction, internal sulfate attack, pyrrhotite, sample preparation

## 1 | INTRODUCTION

Concrete is the most widely used construction material worldwide. Apart from residential homes, concrete is also abundantly applied for the construction of bridges, highways, and skyscrapers. It is therefore necessary to ensure the durability of such vital structures. However, a main cause for the premature degradation of concrete structures has been linked to internal sulfate attack (ISA).<sup>1–5</sup> ISA is a process, which is triggered by the oxidation of sulfide-containing aggregates in concrete releasing free sulfate ions. These free sulfate ions then react with the present phases in hardened concrete to form expansive secondary products like gypsum, delayed ettringite or thaumasite.

Pyrrhotite ( $\text{Fe}_{1-x}\text{S}$ ,  $0 \leq x \leq 0.125$ ) is second to pyrite ( $\text{FeS}_2$ ) the most common source of iron sulfide in

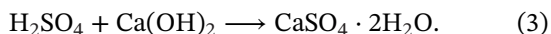
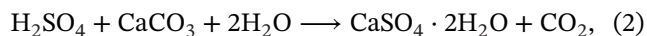
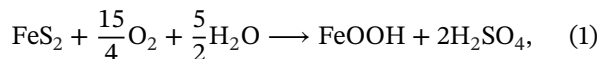
natural aggregates.<sup>6</sup> Even in small amounts ( $< 1 \text{ wt}\%$ ), pyrrhotite can lead to catastrophic concrete material deterioration.<sup>2,7,8</sup> Volume expansion from the oxidation of iron sulfides induces stress, which can cause the formation of cracks throughout the concrete. This compromises the material strength and ultimately the structural integrity, for example, of basement walls.<sup>4,9–11</sup> As a case in point, a recent study reported that the compressive strength of concrete may decrease by 27–100% due to ISA.<sup>4</sup>

Oxidation of an iron sulfide such as pyrrhotite or pyrite, in the presence of water and oxygen, produces sulfuric acid as shown in Equation (1). This is a primary phenomenon that starts a series of destructive secondary reactions in hardened concrete.<sup>5</sup> Sulfuric acid is a key reactant in the formation of expansive gypsum. As detailed in Equations (2) and (3), gypsum can be formed from

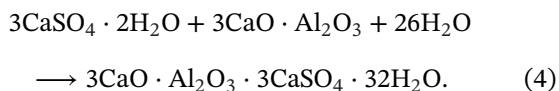
This is an open access article under the terms of the [Creative Commons Attribution-NonCommercial-NoDerivs](https://creativecommons.org/licenses/by-nc-nd/4.0/) License, which permits use and distribution in any medium, provided the original work is properly cited, the use is non-commercial and no modifications or adaptations are made.

© 2021 The Authors. *International Journal of Applied Ceramic Technology* published by Wiley Periodicals LLC on behalf of American Ceramics Society

either a reaction of sulfuric acid with calcite in carbonate aggregates or from a reaction of sulfuric acid with portlandite.<sup>5</sup>



Another common secondary reaction that leads to ISA is the formation of secondary (delayed) ettringite ( $3\text{CaO} \cdot \text{Al}_2\text{O}_3 \cdot 3\text{CaSO}_4 \cdot 32\text{H}_2\text{O}$ ), which is also expansive and has been associated with concrete degradation.<sup>4,11</sup> As illustrated in Equation (4), the reactants are gypsum, water, and aluminates ( $3\text{CaO} \cdot \text{Al}_2\text{O}_3$ ) in the concrete matrix. In the presence of a carbonate and silicate ion source, thaumasite is also formed.<sup>2,12,13</sup>



It is important to note that secondary ettringite forms later in hardened concrete after most of the primary ettringite has already decomposed to monosulfate and gypsum.<sup>3,5,14,15</sup>

The problem of premature concrete degradation due to ISA has been reported from several countries around the world, including the United States,<sup>11,16</sup> Canada,<sup>17</sup> Spain,<sup>8,18</sup> Switzerland,<sup>7</sup> and South Africa.<sup>19</sup> The present study particularly investigates this problem in eastern Connecticut, USA. For more than 25 years, foundations of thousands of homes in this region were constructed with concrete that had pyrrhotite-containing aggregates from a local quarry.<sup>4,16</sup> Temperatures in eastern Connecticut reach average lows of about  $-8^\circ\text{C}$  in winter, and average highs of  $28^\circ\text{C}$  in summer.

Since pyrrhotite is one of the most destructive sources of sulfide ions in aggregates, it is necessary to establish a reliable and efficient procedure to investigate concrete for aggregates that cause ISA. Techniques that have been used to study ISA of concrete include X-ray diffraction (XRD),<sup>20</sup> X-ray fluorescence,<sup>4</sup> scanning electron microscopy (SEM),<sup>11,12</sup> and energy dispersive X-ray spectroscopy (EDS).<sup>4</sup> Of these techniques, XRD is the oldest and most commonly used one for analyzing mineral phases.<sup>4,5,20,21</sup> However, a common disadvantage of XRD is its inability to detect low-phase concentrations ( $< 5\text{ wt}\%$ ), especially in very heterogeneous materials.<sup>4,12,17,21,22</sup> Therefore, XRD is insufficient for the comprehensive characterization of a deleterious mineral like pyrrhotite in concrete aggregates. By contrast, elec-

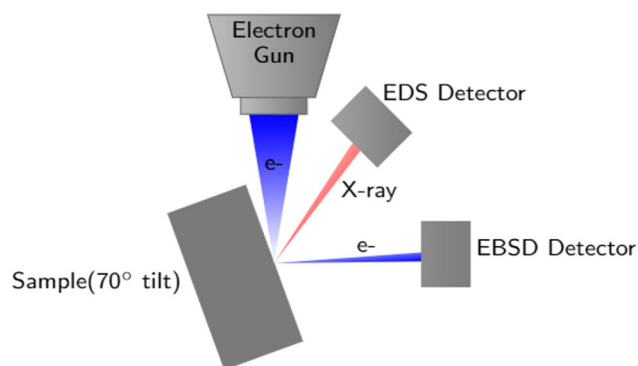


FIGURE 1 A schematic of the equipment setup showing the simultaneous use of EDS and EBSD detectors in the SEM

tron backscatter diffraction (EBSD) provides high spatial and angular resolutions of 20 nm and  $0.5^\circ$ , respectively, and can be automated to obtain reliable statistical representation of the materials.<sup>22–26</sup> Moreover, an EBSD detector can be installed in common scanning electron microscopes and applied in conjunction with the EDS detector as illustrated in Figure 1. These attributes give EBSD a unique position in reliably characterizing and locally quantifying pyrrhotite in concrete.

Studies on concrete often require a simultaneous examination of multiple phases with varying hardness, which poses a challenging need for an enhanced sample preparation method. Moreover, the choice of sample preparation affects the quality and readability of EBSD results.<sup>27</sup> Traditionally, sample preparation (grinding or polishing) and indexing of crystal orientations were performed manually.<sup>28</sup> However, manual methods are not only tedious but lead to variant results based on the user. This study presents the automated sample preparation and indexing of EBSD crystal orientations. A vibratory polishing step was included because it previously improved the quality of EBSD patterns significantly.<sup>22,29</sup>

In previous studies, EBSD was applied to study the expansion-induced cracking caused by alkali silica reactions (ASR).<sup>25,26</sup> ASR and ISA are currently the two main causes for the expansion of concrete structures.<sup>3</sup> ASR is predominant in concrete with aggregates containing amorphous silica, while ISA is more prevalent in concrete with aggregates containing iron sulfides like pyrrhotite and pyrite. In a recent study, EBSD was utilized to characterize aggregates that were at risk for ASR by measuring quartz grain boundaries and crystallographic misorientation.<sup>25</sup> It was demonstrated that in a high pH environment like concrete, the dissolution of deformed quartz occurs not only at high angle grain boundaries but also at subgrain boundaries and Dauphiné twin boundaries. Furthermore, a similar study reported that grain boundary migration in quartz can be linked to changes in crystal lattice orientations.<sup>30</sup> It is important to understand

microstructure changes associated with aggregate deformation because it impacts concrete durability. EBSD is one of the few techniques that makes it possible to recognize and quantify easy-to-miss features such as Dauphiné twin boundaries. It therefore allows the identification of aggregates that are at risk for ASR which may otherwise be missed by standard tests.<sup>25,30</sup> However, while ASR has been well studied,<sup>2,9,10,25</sup> there is no known application of EBSD to understand the specific role of pyrrhotite in ISA.

Based on the above analysis, the goals of this study are, first, to develop an automated method for efficient and reliable preparation of concrete samples using EBSD. The second aim is to use this method to study the oxidation of iron sulfides including pyrrhotite. It is hypothesized that the oxidation of pyrrhotite-containing aggregates in hardened concrete results in secondary expansive products like ettringite, thaumasite, and gypsum, which induce stress in the concrete. If these tensile stresses exceed the tensile strength of the matrix or the matrix-aggregate interfacial transition zone (ITZ), then cracking occurs. To investigate this hypothesis, elements and phases around cracked regions were examined using a SEM that was equipped with EBSD and EDS.

## 2 | EXPERIMENTAL METHODS

### 2.1 | Materials

The current investigation involved concrete cores from slab foundations and walls of seven houses around eastern Connecticut, USA, with varying degrees of deterioration. The sampling method for the concrete cores was described in an earlier study, in which over 70 cores with a diameter of 7.62 cm and a length of 7.62–17.78 cm were collected.<sup>4</sup> In the present work, 10 samples were obtained from five blind cores, respectively, to examine the efficiency of the EBSD method to analyze deleterious pyrrhotite. We wanted to examine if EBSD analysis could reliably characterize which concrete samples contained destructive iron sulfides, without having much information about the concrete beforehand. This method minimized the bias regarding the blind EBSD test.

### 2.2 | Sample preparation

The samples were sectioned to 1.0 cm × 1.0 cm × 0.5 cm each, using a brick saw (Chicago Electric, USA) operating at 400 rpm. All samples were then cold-mounted with an epoxy resin (Epothin2, Buehler, USA). The mounts had a 3.18-cm diameter, which fit in the sample preparation equipment. An automated machine (MetPrep 3, Allied High Tech Products, USA) was used for grinding and polishing. These carefully devised settings along with the necessary consumables are summarized in Table 1.

EBSD analysis requires a thorough surface preparation to flatten the sample and to remove scratches or contamination because these can greatly interfere with indexing of the diffraction patterns. The used equipment allowed the simultaneous preparation of four samples, which made the procedure time efficient. The power head applied a single force of 22 N distributed uniformly among the four samples. The stage on which the abrasive disk was placed is referred to as the platen. Silicon carbide (SiC) grinding papers of US 180 grit, 320 grit, and 600 grit were successively used for 4 min, 6 min, and 4 min, respectively (steps 1–3 in Table 1). Afterwards, the samples were polished with polycrystalline diamond suspensions (Allied High Tech Products, USA) of 6 and 1 μm for 8 min each (steps 4 and 5) to remove the defects left from grinding. The abrasive suspension and a lubricant (Redlube, Allied High Tech Products, USA) were squirted on the polishing cloth (White Label, Allied High Tech Products, USA), every 15 s during polishing, whereas the lubricant minimized friction.

Between each grinding and polishing step, the samples were carefully rinsed with water and dried with compressed air to prevent cross-contamination. Similarly, the equipment power head that held the samples was also wiped down between the successive sample preparation steps. The final polishing step was carried out with an abrasive 0.04 μm noncrystallizing colloidal silica (Allied High Tech Products, USA) for 4 min (step 6) with the aforementioned MetPrep3. In this step, no lubricant was needed but water was applied to presoak and rinse the polishing cloth after use. Until step 6, the total sample preparation time on the MetPrep3 was only 35 min as displayed in Table 1. Nonetheless, additional vibratory polishing is particularly suitable to obtain high-quality EBSD images and crystallographic patterns.<sup>22,29</sup> Therefore, the samples were transferred to a vibratory polisher (Giga 1200, Pace Technologies, USA) and polished for an extra 20 h with colloidal silica. After polishing, the samples were rinsed with water and put in an ultrasonic bath of ethanol to remove any remaining surface residue.<sup>31</sup>

### 2.3 | Microstructure analysis

Microstructure analysis of the concrete samples was performed in an SEM (FEI Teneo, USA), equipped with an EDS detector (Octane Elect Plus, USA) and an EBSD detector (Hitari EBSD, EDAX Inc., USA). Modern SEMs now contain multiple out-lens and in-lens detectors, which filter the signal based on varying kinetic energy and emission angles. This filtering provides enhanced contrast and visualization of features which would otherwise have been missed in an unfiltered image.<sup>32,33</sup> An in-lens detector called Trinity (T1) was applied in this study because it produced minimally charged back scatter electron images of the nonconductive samples.<sup>33</sup> To further mitigate

**TABLE 1** A devised procedure for automatic grinding and polishing of concrete samples on the MetPrep3 equipment. Symbols for the sample and platen: corotating ( $\odot/\odot$ ), and counterrotating ( $\odot/\ominus$ ). Steps 1 and 2 are for grinding, while steps 4–6 are for polishing

Step	Grinding			Polishing		
	1	2	3	4	5	6
Abrasive size	180 grit	320 grit	600 grit	6 $\mu\text{m}$	1 $\mu\text{m}$	0.04 $\mu\text{m}$
Abrasive	SiC	SiC	SiC	Poly diamond	Poly diamond	Colloidal silica
Polishing	-	-	-	White Label	White Label	Chem-pol
Lubricant	Water	Water	Water	Redlube	Redlube	-
Platen (RPM)	300	300	300	150	150	150
Direction	$\odot/\odot$	$\odot/\odot$	$\odot/\odot$	$\odot/\ominus$	$\odot/\odot$	$\odot/\odot$
Sample (RPM)	150	150	150	150	150	150
Force (N)	22	22	22	22	22	22
Time (min)	4	6	4	8	8	4

charging, copper tape was wrapped around edges of the sample mounts prior to imaging. The working distance in the vertical direction was 14–15 mm. Each prepared sample was then loaded on the 45° pretilted stage in the SEM and was set to tilt an additional 25° for a total tilt angle of 70°. This angle optimizes electron diffraction and constructive interference, which produce diffraction lines (Kikuchi bands) that represent the crystallographic planes in the sample.<sup>34</sup> Detected Kikuchi bands from the image are reconstructed in the Hough space to find the highest peak intensity.<sup>35</sup> Interplanar angles between three intersecting bands are then calculated and compared in a database table for Miller indices (*hkl*) of similar crystal structures to identify and index the pattern.

We solved the EBSD patterns using an automated indexing software called orientation imaging microscopy (EDAX, USA). A phase list was specified for the software to search for pyrrhotite, pyrite, gypsum, ettringite, quartz, and calcite. Other key phases that were reported in the literature about ISA due to pyrrhotite oxidation were also added, including albite, biotite, thenardite and aphtitalite.<sup>4,5</sup> A visual representation of how EBSD patterns were obtained is displayed in Figure 2. The EBSD detector was inserted horizontally to be 2.0 mm away from the sample. A voltage of 20 kV and a current of 1.6 nA were applied. EBSD crystallography and EDS elemental analysis were performed simultaneously, which ensured accuracy and time efficiency.

EBSD investigations were performed under high vacuum ( $7.3 \times 10^{-4}$  Pa) because it demonstrates higher diffraction intensity (and higher confidence index (CI) than low vacuum.<sup>36</sup> CI is defined as a measure of how reliable the EBSD indexing method is above a set tolerance value (usually 0.1).<sup>37</sup> To obtain high-quality EBSD indices, the baseline parameters should be at least six bands to index and a CI greater than 0.1 should be attained, respectively.<sup>25</sup> For further accuracy, we ensured that an

image quality (IQ) of  $\geq 2500$  and a fit of  $\leq 2^\circ$  were obtained as seen in Figure 3. Thereby, IQ is a measurement of the precision of EBSD patterns. The IQ of a sample is heavily influenced by any crystallographic irregularity such as defects, strain, and phase boundaries.<sup>34</sup> A low IQ, thus, results in blurry band edges and a low band contrast. Therefore, we examined each SEM image for high IQ, excellent CI, and sharp EBSD patterns before generating a report.

### 3 | RESULTS AND DISCUSSION

#### 3.1 | Evaluation of the devised sample preparation procedure

A key purpose of this study was the optimization of the concrete sample preparation and to examine the ISA in the prepared samples. We first compared the devised sample preparation procedure to standard grinding and polishing. Furthermore, the EBSD band clarity before and after sputter coating was also evaluated. Second, the optimum vacuum mode for backscatter electron was analyzed. Lastly, secondary reaction products that could form from oxidation of iron sulfides were investigated.

Attaining EBSD-quality surfaces using standard (manual) ceramographic procedures for concrete is often a challenge and the success highly user-dependent. The sample preparation procedure presented in this study was not only more time efficient, but the automation ensured similar results despite being carried out by different users. While automation is not new, until now there was no published procedure for a fully automated preparation method of concrete samples for ISA analysis using EBSD. Interestingly, our method enabled clear examination of feldspar on a relatively thick sample as observed from Figure 4. Previously, some studies had to perform

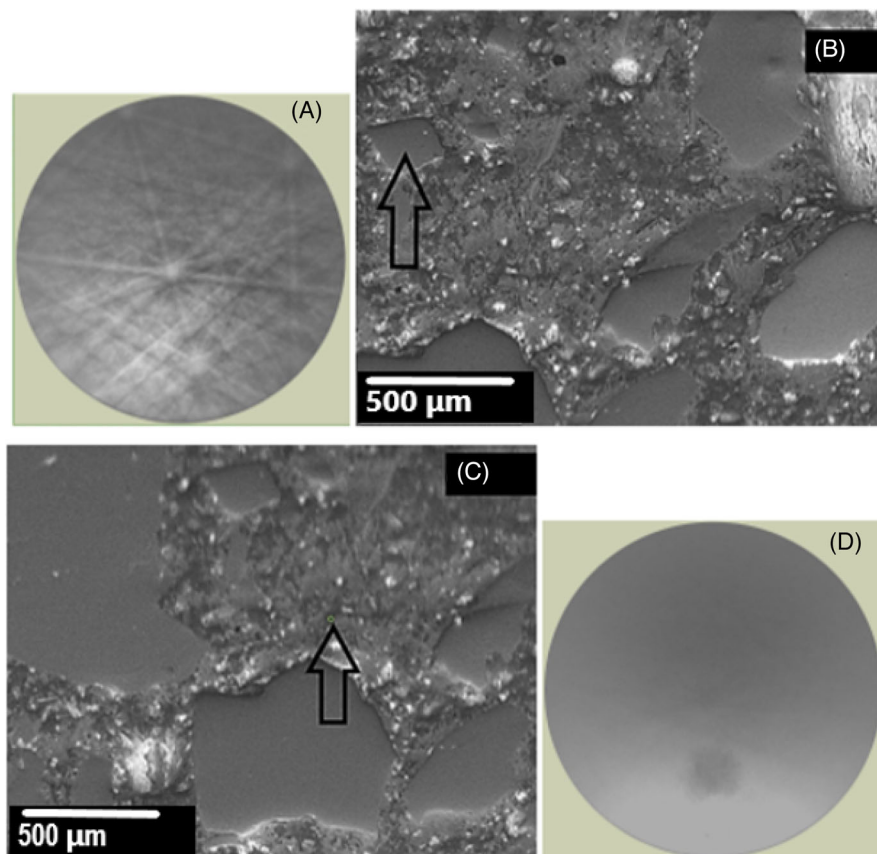


**FIGURE 2** A visual description of how EBSD patterns were obtained. A crystalline region showed Kikuchi bands as seen in (A). Crystalline regions in BSE images were mainly from aggregates as shown in (B). Amorphous regions were largely from the cement paste as seen in (C), which produced no diffraction patterns (D). Even though these images are from the blind core 2 sample, this identification pattern was similar in all other samples

petrography (thin sectioning) to analyze feldspar in concrete.<sup>5</sup>

Sputter coating of a nonconductive sample like concrete, with a layer of carbon, conductive glass, or a metallic coating is commonly applied to mitigate surface charging. The main potential drawback of sputter coating, however, is the inclusion of the coating material in the EBSD patterns. Furthermore, since EBSD is a surface technique, there is a high probability of the Kikuchi bands being obstructed by the coating. This study compared EBSD analysis of samples sputtered with a standard 2-nm Au-Pd coating to those with no coating. Backscattered-electron (BSE) images of the sputtered samples had minimal charging, but more reliable EBSD patterns were obtained from the nonsputtered samples as portrayed in Figure 5.

Second, we observed that EBSD patterns were significantly diminished in sputter-coated samples compared to the nonsputtered ones as displayed in Figure 5. Since EBSD analyzes the top 100 nm of the sample, the sputter coating can obstruct a significant number of Kikuchi bands. During the comparison analysis, we used a sputter coating of 2 nm Au-Pd, because metallic coatings often outper-

form carbon coatings.<sup>22</sup> Additionally, a coating of 2.5 nm or less is suggested, with unsatisfactory EBSD patterns from samples with coating thicknesses larger than 5 nm.<sup>36</sup> Overall, we recommend avoiding sputter coating on EBSD samples and to use the T1 in-lens detector instead to minimize charging.

### 3.2 | Optimum vacuum mode for backscatter electron imaging

It was vital to analyze the ITZ between the aggregates and the hardened cement matrix of the concrete because this region is often reported to contain high porosity, fully reacted clinker phases, and oxidation expansion products like ettringite.<sup>4,38</sup> As shown in Figure 6A, there was evident porosity in the ITZ. Additionally, thaumasite bands—similar to those identified by Yang and Buenfeld<sup>12</sup>—were observed at the ITZ (Figure 6B). A summary of the minerals characterized from all the samples using EBSD crystallography is displayed in Table 2.

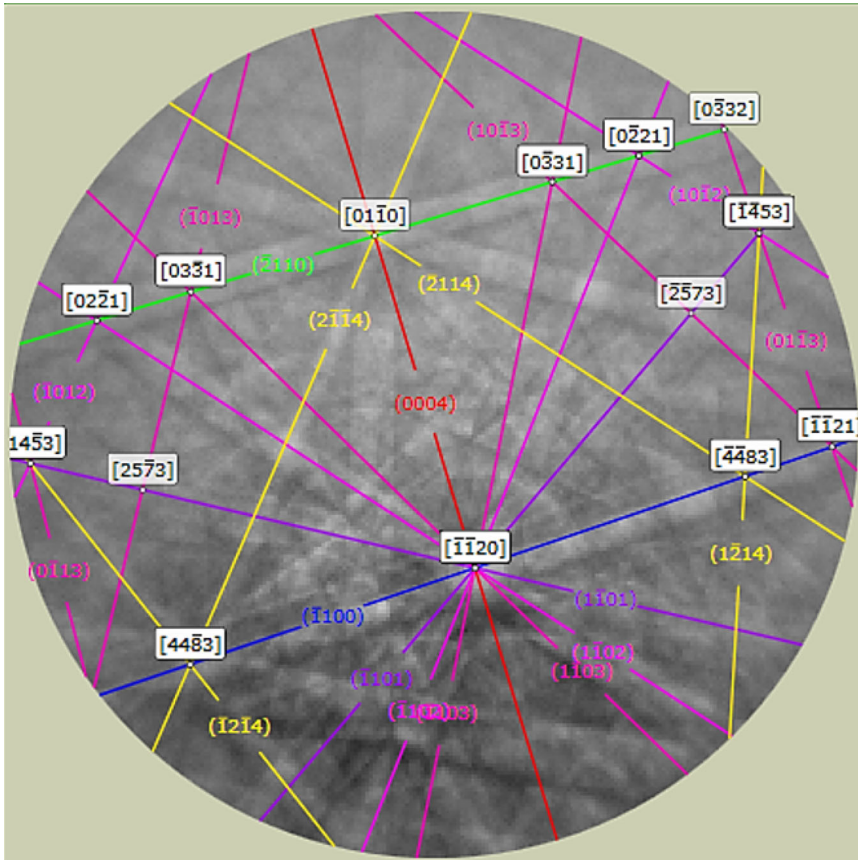


**FIGURE 3** EBSD crystallography of pyrrhotite in the sample from blind concrete core 1. The values obtained for this region were an IQ of 3803.7, a CI of 0.1, and a fit of 1.5°. While there were some unmatched bands in this pattern, the obtained values for IQ, CI, and fit meet a high accuracy standard, that is, six or more indexed bands, CI  $\geq 0.1$ , IQ of  $\geq 2500$ , and a fit  $\leq 2^\circ$

**TABLE 2** Mineral phases characterized from the blind concrete cores using EBSD crystallography

Core number	Key phase identified	Phase symmetry
Core 1	Pyrrhotite, Fe <sub>0.96</sub> S	Hexagonal ( <i>D6h</i> ) [ <i>6/mmm</i> ]
	Marcasite, FeS <sub>2</sub>	Orthorhombic ( <i>D2h</i> ) [ <i>mmm</i> ]
	Pyrite, FeS <sub>2</sub>	Cubic ( <i>Oh</i> ) [ <i>m3m</i> ]
	Gypsum, CaSO <sub>4</sub> · 2H <sub>2</sub> O	Monoclinic b ( <i>C2h</i> ) [ <i>2/m</i> ]
	Quartz, SiO <sub>2</sub>	Trigonal ( <i>D3d</i> ) [ <i>-3m</i> ]
	Biotite, K <sub>2</sub> (Mg Fe Al) <sub>2</sub> [Si <sub>4</sub> Al <sub>4</sub> O <sub>20</sub> ]	Monoclinic b ( <i>C2h</i> ) [ <i>2/m</i> ]
	Albite, (Na <sub>0.84</sub> Ca <sub>0.16</sub> )Al <sub>1.16</sub> Si <sub>2.84</sub> O <sub>8</sub>	Triclinic ( <i>S2, Ci</i> ) [ <i>-1</i> ]
	Calcite, CaCO <sub>3</sub>	Trigonal ( <i>D3d</i> ) [ <i>-3m</i> ]
	Core 2	Pyrite, FeS <sub>2</sub>
Marcasite, FeS <sub>2</sub>		Orthorhombic ( <i>D2h</i> ) [ <i>mmm</i> ]
Pyrrhotite, Fe <sub>0.96</sub> S		Hexagonal ( <i>D6h</i> ) [ <i>6/mmm</i> ]
Core 3	Biotite, K <sub>2</sub> (Mg Fe Al) <sub>6</sub> [Si <sub>4</sub> Al <sub>4</sub> O <sub>20</sub> ]	Monoclinic b ( <i>C2h</i> ) [ <i>2/m</i> ]
	Calcite, CaCO <sub>3</sub>	Trigonal ( <i>D3d</i> ) [ <i>-3m</i> ]
	Quartz, SiO <sub>2</sub>	Trigonal ( <i>D3d</i> ) [ <i>-3m</i> ]
Core 4	Quartz, SiO <sub>2</sub>	Trigonal ( <i>D3d</i> ) [ <i>-3m</i> ]
	Argonite, CaCO <sub>3</sub>	Orthorhombic ( <i>D2h</i> ) [ <i>mmm</i> ]
	Omphacite, (Ca,Na)(Mg,Fe,Al)[Si <sub>2</sub> O <sub>6</sub> ]	Monoclinic b ( <i>C2h</i> ) [ <i>2/m</i> ]
	Biotite, K <sub>2</sub> (Mg Fe Al) <sub>6</sub> [Si <sub>4</sub> Al <sub>4</sub> O <sub>20</sub> ]	Monoclinic b ( <i>C2h</i> ) [ <i>2/m</i> ]
Core 5	Pyrrhotite, Fe <sub>0.96</sub> S	Hexagonal ( <i>D6h</i> ) [ <i>6/mmm</i> ]
	Marcasite, FeS <sub>2</sub>	Orthorhombic ( <i>D2h</i> ) [ <i>mmm</i> ]

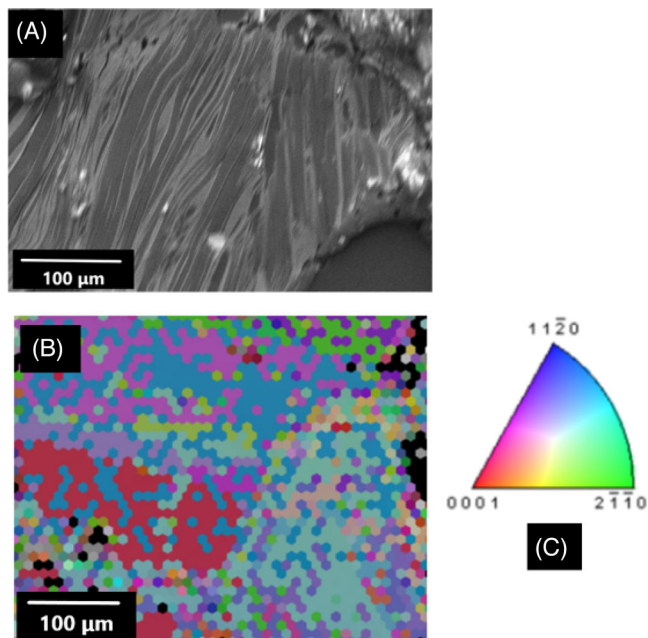


**FIGURE 4** EBSD analysis of the sample from blind concrete core 1 revealing (A) the prominent presence of feldspar (stripe-like structures), (B) crystal orientation mapping, and (C) map legend for hexagonal lattice planes

We found an advantage of low vacuum SEM (LVSEM) over high vacuum SEM (HVSEM) because it resulted in less charging of the nonconductive concrete samples (see Figure 7). Backscatter electron imaging is recommended over secondary electron imaging for better contrast. Blurry bands in EBSD patterns, however, are the primary drawback of LVSEM. Therefore, LVSEM investigations were carried out independently of EBSD crystallography. During vacuum mode optimization analysis, standard SEM parameters were applied including placing the samples on the flat stage and a 10-mm working distance, instead of the EBSD tilted stage or a 15-mm working distance. Particularly, the only parameter that was different between LVSEM and HVSEM, was the pressure—10 Pa

versus  $7.3 \times 10^{-4}$  Pa, respectively. The current and voltage were kept constant which enabled a direct comparison.

### 3.3 | Investigation of secondary reaction products

We observed and locally quantified destructive iron sulfides, particularly pyrrhotite, pyrite, and marcasite using EBSD and EDS. EBSD analysis of crystalline regions showed defined Kikuchi bands, but amorphous regions showed no diffraction as portrayed in Figures 2 and 3. Interestingly, the aforementioned iron sulfides can coexist as mapped in Figure 8. These iron sulfides are associated with ISA. They were characterized in several samples as displayed in Figures 8 and 9 and Table 2. Marcasite ( $\text{FeS}_2$ ) is a polymorph of pyrite with an orthorhombic crystal structure, instead of the typical cubic pyrite structure as demonstrated in Figure 9. This distinction is important because marcasite is less stable than pyrite<sup>39,40</sup> and could thus oxidize more readily than pyrite. Thus, our EBSD method not only identified just pyrrhotite but notably also other destructive iron sulfides, particularly pyrite and marcasite.

EBSD analysis of the sample from blind concrete core 1 revealed the highest quantified amount of pyrrhotite (Figure 8). It also had gypsum, a calcium aluminate phase (Figure 10), and significant amounts of feldspar (Figure 4). Feldspar is a common phase in both fine and coarse aggregates, particularly those obtained from river sand and graywackes, respectively. Notably, meta-graywackes can be a source of pyrrhotite,<sup>41</sup> which agrees with the fact that blind concrete core 1 contained pyrrhotite as revealed in Figure 8. It was important to examine regions where pyrrhotite was in contact with micas like biotite because the coexistence of these phases was reported to accelerate oxidation.<sup>5</sup> As shown in Table 2, concrete cores 1, 3, and 4 were all identified to contain biotite. However, only core 1 had both pyrrhotite and biotite, but these minerals were not observed to be in contact.

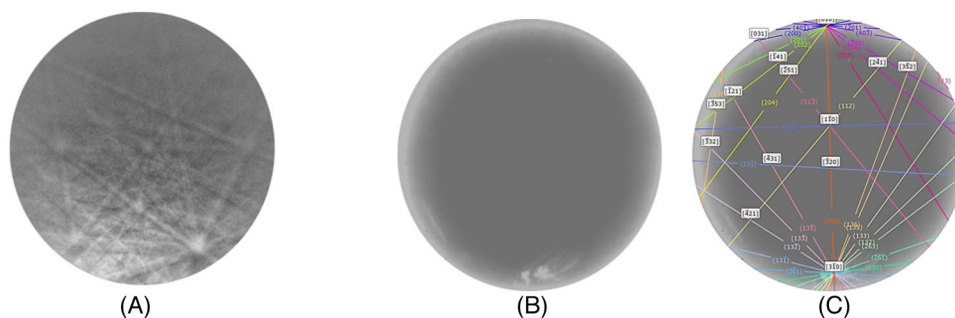


**FIGURE 5** EBSD crystallography of biotite from a non-sputtered sample (A), compared to a 2-nm Au-Pd sputtered sample (B). Indexed patterns of non-sputtered samples (A) were clearer and more reliable than those from sputter-coated samples (B) and (C)

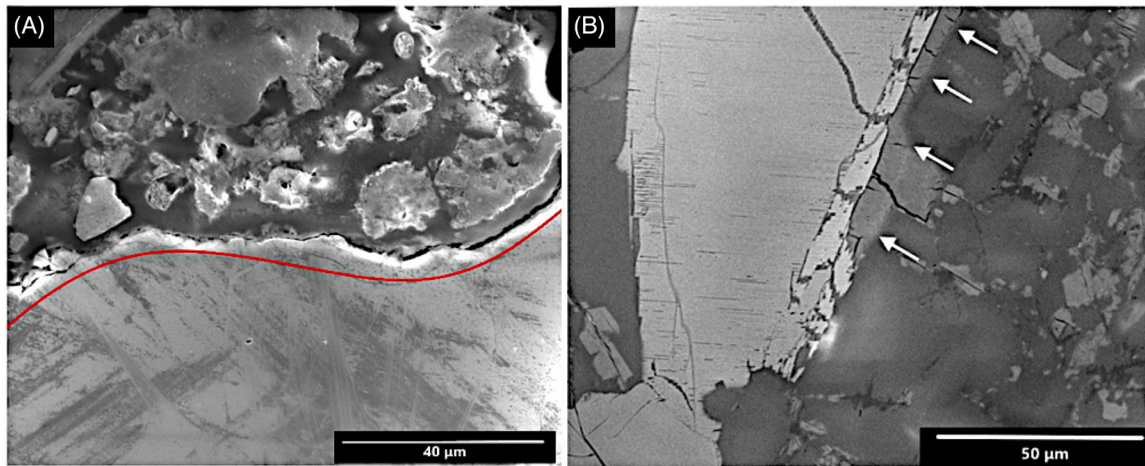


**FIGURE 6** Investigation of the ITZ in the sample from blind concrete core 1. As seen in (A), this boundary region between the aggregate and the cement matrix has a particularly high porosity. The arrows indicate bands believed to be thaumasite (B)

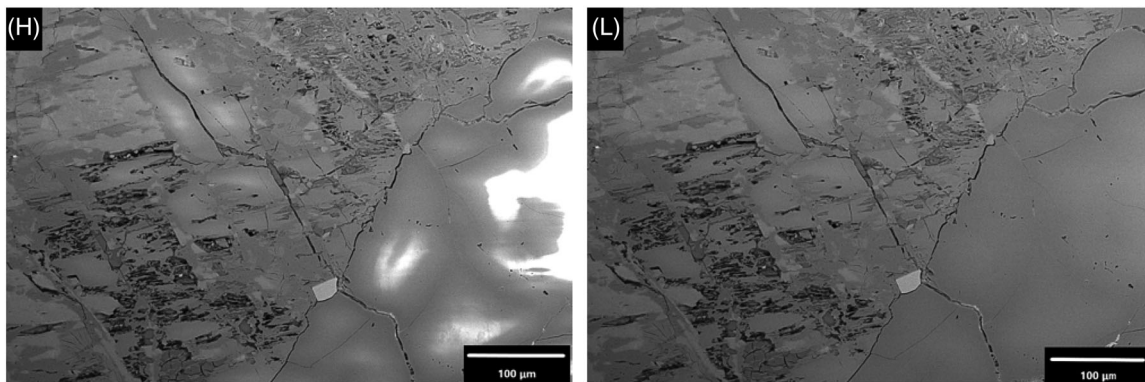


**FIGURE 7** Investigation of the optimum vacuum mode for backscatter electron imaging. High vacuum mode (H) had more charging than low vacuum mode (L). The difference is seen in the right-hand side of both images

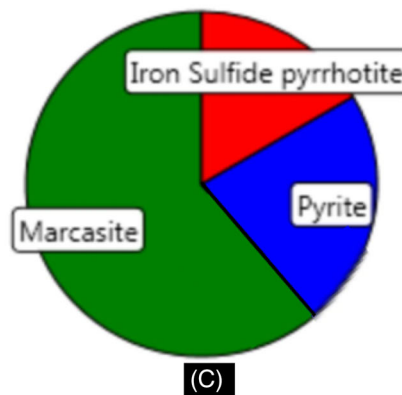
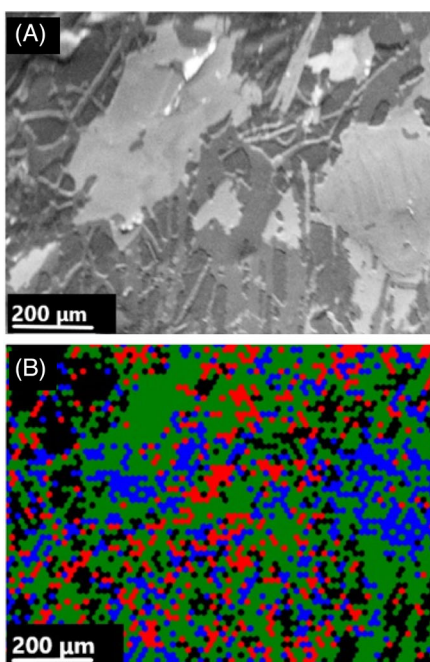


**FIGURE 8** (A) Backscatter electron image of the sample from blind concrete core 1, (B) EBSD phase distribution, and (C) phase quantification. In this region, there was 22% pyrite ( $\text{FeS}_2$ -cubic), 61% marcasite ( $\text{FeS}_2$ -orthorhombic), and 17% pyrrhotite ( $\text{FeS}$ ). Phase compositions were obtained using the method of EBSD mapping

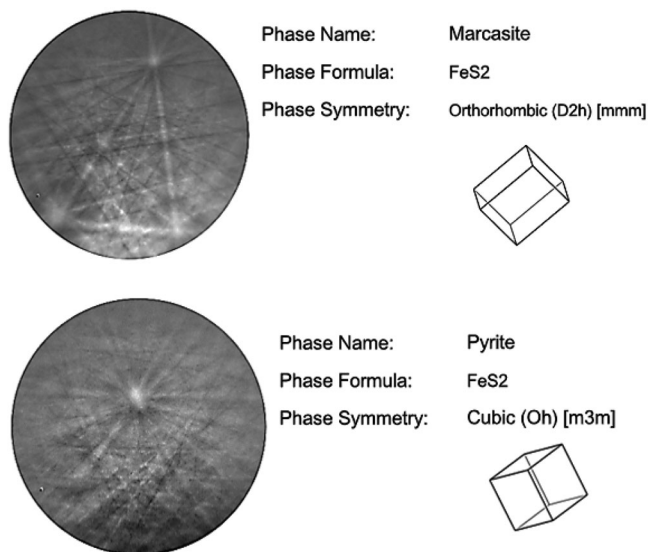


**FIGURE 9** Comparison between the crystal structures of marcasite and pyrite. Marcasite is a polymorph of pyrite with an orthorhombic crystal structure, but the common crystal structure of pyrite is cubic. Marcasite is less stable than pyrite and could thus oxidize more rapidly in the presence of water and oxygen. The EBSD examination revealed marcasite in samples from blind cores 1, 2, and 5

Secondary ettringite [3CaO · Al<sub>2</sub>O<sub>3</sub> · 3CaSO<sub>4</sub> · 32H<sub>2</sub>O] and thaumasite [CaSiO<sub>3</sub> · CaCO<sub>3</sub> · CaSO<sub>4</sub> · 15H<sub>2</sub>O] are known to be needle like.<sup>4,13</sup> The EDS chemical analysis of needle-like features in the sample from blind concrete core 3 (Figure 11) revealed some component elements like calcium, aluminum, and silicon. A line map of elemental components across a crack fissure in the same sample also revealed the presence of sulfur and carbon. Notably, cracks

or pores provide space for the expansion of secondary reaction products. EBSD results of this sample (Table 2), however, did not reveal iron sulfide phases. Therefore, the iron and sulfur identified by EDS might have been present in the matrix due to the general clinker composition. Additionally, ettringite might be found in concrete after advanced aging and might not be necessarily connected with the attack by sulfates. For example, in Table 2 core 3 did not contain any iron sulfides.

Figure 11 is an image analysis of long needle-like features in the sample from blind concrete core 3. These features were of high interest because thaumasite and ettringite are microscopically needle like.<sup>4,13</sup> We also observed crack fissures in this sample as portrayed in Figure 12. Interestingly, even though elemental iron and sulfur were mapped in this area using EDS, EBSD did not reveal iron sulfide phases such as pyrrhotite, pyrite, or marcasite (see Table 2). We performed additional XRD analysis on this sample, but there was no reliable indication of thaumasite and ettringite, either. Therefore, the elemental iron and sulfur mapped by EDS are most likely from the biotite and sulfate phases identified using EBSD (Table 2). Furthermore, the crack fissures can sometimes be from weathering, sample extraction, or sectioning.

The sample from blind concrete core 5 was the most deteriorated of all the samples, as shown by the cracks in Figure 13A. Upon investigation, it was observed that strong peaks of iron and sulfur were evident in the heavily cracked region (see Figure 13B). In other areas of this sample, iron-rich aggregates were prominent as indicated in Figure 14. EBSD analysis of this significantly deteriorated sample highlighted iron sulfide minerals—pyrrhotite and marcasite—as displayed in Table 2. Marcasite (FeS<sub>2</sub>) is

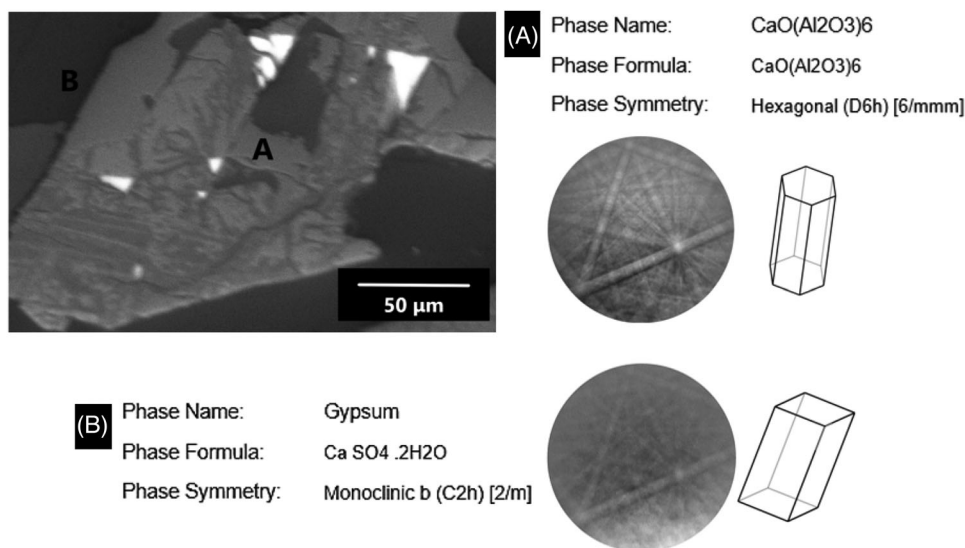


**FIGURE 10** Diffraction results from the BSE image of the sample from blind concrete core 1, showing a calcium aluminate phase from region A and gypsum from region B

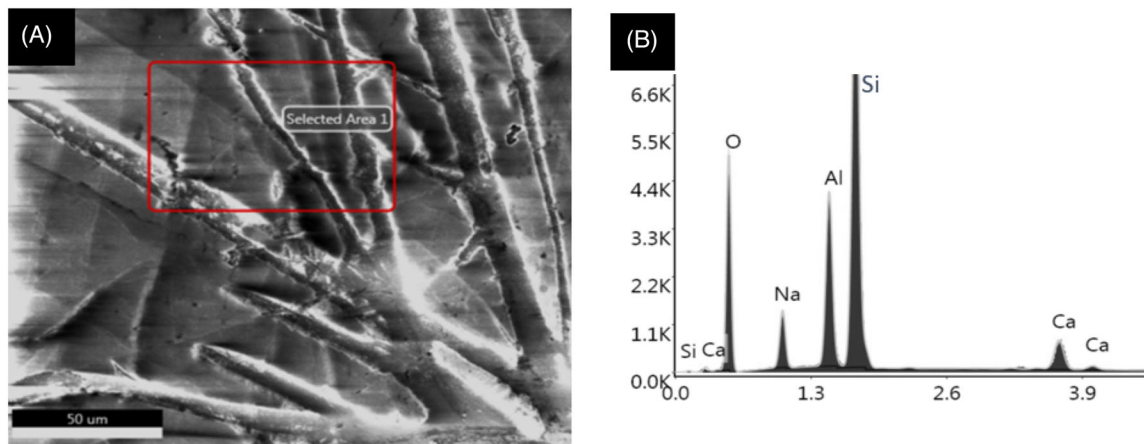


FIGURE 11 Secondary electron image of needle-like features in the sample from blind concrete core 3 (A) and a histogram of elements in the area indicated (B)

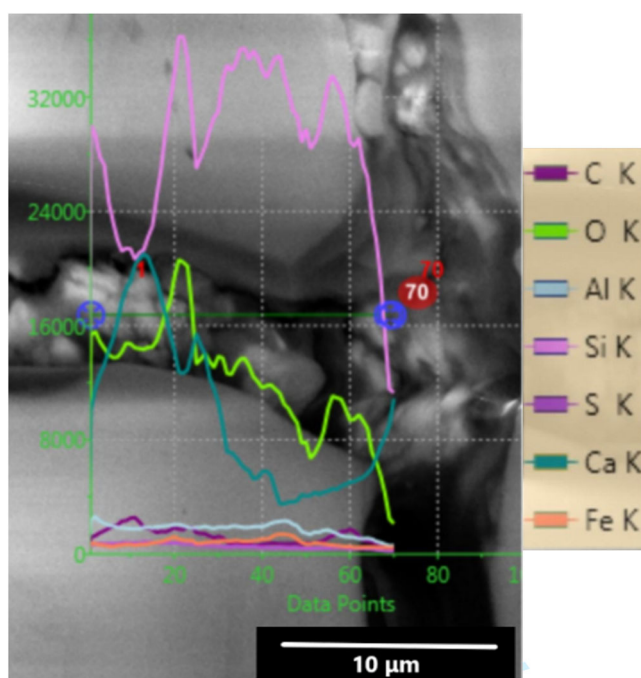


FIGURE 12 Line map showing the elemental components around a crack fissure in the sample from blind concrete core 3. Even though elemental iron, sulfur, and oxygen were mapped in this area using EDS, EBSD did not reveal iron sulfide phases like pyrrhotite or pyrite. Thus, this cracking could be from weathering, sample extraction, or sectioning

a polymorph of pyrite with an orthorhombic crystal structure, instead of the typical cubic pyrite structure as demonstrated in Figure 9. This distinction is important because marcasite is less stable than pyrite<sup>39,40</sup> and can thus oxidize more readily than pyrite.

Overall, an important aspect of the method presented in this paper is characterization and local quantification of potentially reactive iron sulfide-bearing aggregates. Some

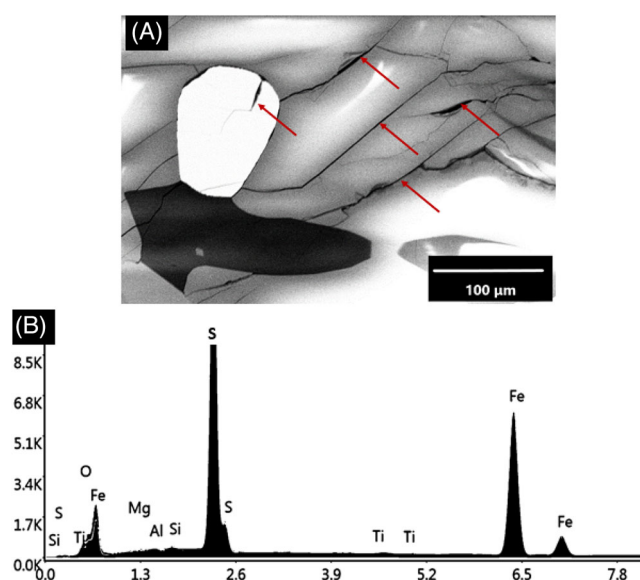
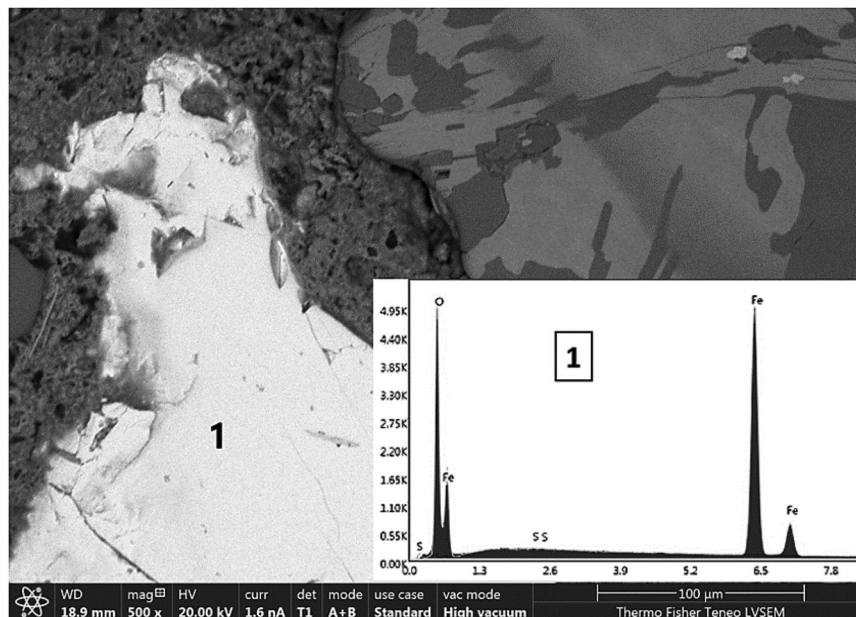


FIGURE 13 BSE image of the sample from blind concrete core 5 showing a heavily cracked region as indicated by the arrows. The EDS histogram (B) in this region showed prominent peaks of iron and sulfur

key phases identified include pyrrhotite, pyrite and marcasite. While EBSD reliably provided the crystal structure of the indexed phase, it sometimes had a limitation of consistently identifying the correct elemental composition. Therefore, EDS was applied alongside EBSD analysis to confirm the indexed minerals. Moreover, sample preparation requirements of EDS are drastically overshadowed by those of EBSD, so samples prepared for EBSD are typically suitable for chemical characterization by EDS. Performing such investigations before the aggregates are used in concrete could save significant costs and time associated with repairing crumbling foundations and cracking walls. Nowadays, aggregates of good quality are becoming scarce

**FIGURE 14** Chemical analysis of the sample from blind concrete core 5 to examine the bright region marked (1) in the BSE image. As indicated by the histogram, this region was a prominently iron-rich area. A similar trend was observed in bright regions of other samples



in areas close to very large cities in the world. Therefore, this method could complement existing standard methods in helping to decide if certain aggregates should or should not be used in concrete mixes.

#### 4 | CONCLUSION

This study presented an automated sample preparation method for concrete samples for the simultaneous EBSD and EDS analysis to characterize and locally quantify mineral phases. Samples were obtained from eastern Connecticut, USA, where thousands of houses are currently at risk for premature concrete degradation. We demonstrated that with our excellent automated surface preparation method and no surface coatings, clear EBSD patterns and crystal orientation maps of minerals around deteriorated regions in the concrete can be observed. Of the mineral phases identified, the most deleterious were pyrrhotite, pyrite, and marcasite, because they are associated with ISA in hardened concrete. The presence of such iron sulfides in concrete can accelerate the degradation of concrete in building foundations. Therefore, early detection and quantification of destructive iron sulfides can enable preventative correction of crumbling foundation problems before they arise. Although EBSD analysis was historically applied in metallurgical crystallography, this work demonstrated that EBSD is a viable technique to analyze and predict ISA in hardened concrete.

#### ACKNOWLEDGMENTS

The authors would like to thank Dr. Kay Wille, from the University of Connecticut, for his insight comments.

Funding for this work was provided by faculty startup funds of the Institute of Material Science and the School of Engineering and through the Scholarship Facilitation Fund of the University of Connecticut.

#### ORCID

Stefan Schafföner  <https://orcid.org/0000-0002-6526-2496>

#### REFERENCES

1. Marcelino AP, Calixto JM, Gumieri AG, Caldeira CL, Delbem ID, Ferreira MC. A feasible evaluation protocol to determine the most reactive sulfide-bearing aggregate for use in concrete. *Constr Build Mater.* 2020;242:118031.
2. Rodrigues A, Duchesne J, Fournier B. A new accelerated mortar bar test to assess the potential deleterious effect of sulfide-bearing aggregate in concrete. *Cem Concr Res.* 2015;73:96–110.
3. Campos A, Lopez CM, Blanco A, Aguado A. Effects of an internal sulfate attack and an alkali-aggregate reaction in a concrete dam. *Constr Build Mater.* 2018;166:668–683. <https://doi.org/10.1016/j.conbuildmat.2018.01.180>
4. Zhong R, Wille K. Deterioration of residential concrete foundations: the role of pyrrhotite-bearing aggregate. *Cem Concr Compos.* 2018;94:53–61.
5. Tagnit-Hamou A, Saric-Coric M, Rivard P. Internal deterioration of concrete by the oxidation of pyrrhotitic aggregates. *Cem Concr Res.* 2005;35:99–107.
6. Belzile N, Chen Y-W, Cai M-F, Li Y. A review on pyrrhotite oxidation. *J Geochem Explor.* 2004;84:65–76.
7. Schmidt T, Leemann A, Gallucci E, Scrivener K. Physical and microstructural aspects of iron sulfide degradation in concrete. *Cem Concr Res.* 2011;41:263–269.
8. Ayora C, Chinchón S., Aguado A, Guirado F. Weathering of iron sulfides and concrete alteration: thermodynamic model and observation in dams from Central Pyrenees, Spain. *Cem Concr Res.* 1998;28:1223–1235.

9. Ju T, Achenbach JD, Cusatis G, Jacobs LJ, Qu J. Wave mixing technique for nondestructive assessment of alkali-silica reaction damage in concrete prism samples. *AIP Conf Proc.* 2019;2102:110004. <https://doi.org/10.1063/1.5099841>
10. Ju T, Achenbach JD, Jacobs LJ, Guimaraes M, Qu J. Ultrasonic nondestructive evaluation of alkali-silica reaction damage in concrete prism samples. *Mater Struct.* 2017;50:60.
11. Lee H, Cody R, Cody A, Spry P. The formation and role of ettringite in Iowa highway concrete deterioration. *Cem Concr Res.* 2005;35:332–343. <https://doi.org/10.1016/j.cemconres.2004.05.029>
12. Yang R, Buenfeld NR. Microstructural identification of thaumasite in concrete by backscattered electron imaging at low vacuum. *Cem Concr Res.* 2000;30:775–779. [https://doi.org/10.1016/S0008-8846\(00\)00244-1](https://doi.org/10.1016/S0008-8846(00)00244-1)
13. Blanco-Varela M, Aguilera J, Martinez-Ramirez S. Effect of cement C3A content, temperature and storage medium on thaumasite formation in carbonated mortars. *Cem Concr Res.* 2006;36:707–715.
14. Liu X, Feng P, Lyu C, Ye S. The role of sulfate ions in tricalcium aluminate hydration: new insights. *Cem Concr Res.* 2020;130:105973. <https://doi.org/10.1016/j.cemconres.2020.105973>
15. Casanova I, Agulló L, Aguado A. Aggregate expansivity due to sulfide oxidation—I. Reaction system and rate model. *Cem Concr Res.* 1996;26:993–998.
16. Geiss CE, Gourley JR. A thermomagnetic technique to quantify the risk of internal sulfur attack due to pyrrhotite. *Cem Concr Res.* 2019;115:1–7.
17. Rodrigues A, Duchesne J, Fournier B, Durand B, Rivard P, Shehata M. Mineralogical and chemical assessment of concrete damaged by the oxidation of sulfide-bearing aggregates: importance of thaumasite formation on reaction mechanisms. *Cem Concr Res.* 2012;42:1336–1347.
18. Chinchón J, López-Soler A, Querol X, Vaquer R. Determination of pyrrhotite ( $\text{Fe}_{1-x}\text{S}$ ) occurring in aggregates by X-ray fluorescence. *Cem Concr Res.* 1990;20:394–397. [https://doi.org/10.1016/0008-8846\(90\)90029-W](https://doi.org/10.1016/0008-8846(90)90029-W)
19. Oberholster R, Krüger J. Investigation of alkali-reactive, sulphide-bearing and by-product aggregates. *Bull Int Assoc Eng Geol-Bulletin de l'Association Internationale de Géologie de l'Ingénieur.* 1980;22:273–277. <https://doi.org/10.1007/BF02600685>
20. Mikhlin YL, Kuklinskiy A, Pavlenko N, Varnek V, Asanov I, Okotrub A, et al. Spectroscopic and XRD studies of the air degradation of acid-reacted pyrrhotites. *Geochim Cosmochim Acta.* 2002;66:4057–4067. [https://doi.org/10.1016/S0016-7037\(02\)00989-4](https://doi.org/10.1016/S0016-7037(02)00989-4)
21. Schafföner S, Aneziris CG, Berek H, Hubáľková J, Rotmann B, Friedrich B. Corrosion behavior of calcium zirconate refractories in contact with titanium aluminide melts. *J Eur Ceram Soc.* 2015;35:1097–1106. <https://doi.org/10.1016/j.jeurceramsoc.2014.09.032>
22. Berek H, Yanina A, Weigelt C, Aneziris C. Determination of the phase distribution in sintered TRIP-matrix/Mg-PSZ composites using EBSD. *Steel Res Int.* 2011;82:1094–1100. <https://doi.org/10.1002/srin.201100064>
23. Borrajo-Pelaez R, Hedström P. Recent developments of crystallographic analysis methods in the scanning electron microscope for applications in metallurgy. *Crit Rev Solid State Mater Sci.* 2018;43:455–474. <https://doi.org/10.1080/10408436.2017.1370576>
24. Zaefferer S. A critical review of orientation microscopy in SEM and TEM. *Cryst Res Technol.* 2011;46:607–628.
25. Rößler C, Möser B, Giebson C, Ludwig H-M. Application of electron backscatter diffraction to evaluate the ASR risk of concrete aggregates. *Cem Concr Res.* 2017;95:47–55.
26. Prior DJ, Boyle AP, Brenker F, Cheadle MC, Day A, Lopez G, et al. The application of electron backscatter diffraction and orientation contrast imaging in the SEM to textural problems in rocks. *Am Mineral.* 1999;84:1741–1759.
27. Halfpenny A, Hough RM, Verrall M. Preparation of samples with both hard and soft phases for electron backscatter diffraction: examples from gold mineralization. *Microsc Microanal.* 2013;19:1007–1018.
28. Wright SI, Adams BL, Kunze K. Application of a new automatic lattice orientation measurement technique to polycrystalline aluminum. *Mater Sci Eng A.* 1993;160:229–240. [https://doi.org/10.1016/0921-5093\(93\)90452-K](https://doi.org/10.1016/0921-5093(93)90452-K)
29. Schafföner S, Aneziris CG, Berek H, Hubáľková J, Priese A. Fused calcium zirconate for refractory applications. *J Eur Ceram Soc.* 2013. <https://doi.org/10.1016/j.jeurceramsoc.2013.07.008>
30. Piazzolo S, Prior D, Holness M. The use of combined cathodoluminescence and EBSD analysis: a case study investigating grain boundary migration mechanisms in quartz. *J Microsc.* 2005;217:152–161.
31. Luo H, Wang X, Dong C, Xiao K, Li X. Effect of cold deformation on the corrosion behaviour of UNS S31803 duplex stainless steel in simulated concrete pore solution. *Corros Sci.* 2017;124:178–192. <https://doi.org/10.1016/j.corsci.2017.05.021>
32. Mikmeková Š, Nakamichi H, Nagoshi M. Contrast of positively charged oxide precipitate in out-lens, in-lens and in-column SE image. *Microscopy.* 2018;67:11–17.
33. Wandrol P, Vašina R, Sandu A, Vesseur EJ, Tüma L. Selective detection of backscattered electrons in the compound lens equipped UHR SEM. *Microsc Microanal.* 2016;22:576–577.
34. Stojakovic D. Electron backscatter diffraction in materials characterization. *Process Appl Ceram.* 2012;6:1–13.
35. Duda RO, Hart PE. Use of the Hough transformation to detect lines and curves in pictures. *Commun ACM.* 1972;15:11–15. <https://doi.org/10.1145/361237.361242>
36. Pérez-Huerta A, Cusack M. Optimizing electron backscatter diffraction of carbonate biominerals—resin type and carbon coating. *Microsc Microanal.* 2009;15:197–203.
37. Wright SI, Nowell MM, Lindeman SP, Camus PP, De Graef M, Jackson MA. Introduction and comparison of new EBSD post-processing methodologies. *Ultramicroscopy.* 2015;159:81–94.
38. Winslow DN, Cohen MD, Bentz DP, Snyder KA, Garboczi EJ. Percolation and pore structure in mortars and concrete. *Cem Concr Res.* 1994;24:25–37.
39. Lennie AR, Vaughan DJ. Kinetics of the marcasite-pyrite transformation: an infrared spectroscopic study. *Am Mineral.* 1992;77:1166–1171. [https://pubs.geoscienceworld.org/msa/ammin/article/77/11-12/1166/42628/Kinetics-of-the-marcasitepyrite-transformation-An?casa\\_token=j8FzrxhbbcAAAA: DydykzhVazgSGF8zLkUd\\_NYcOLy6w0qLEZNMsoCUGzQRIO\\_wzMJq\\_7g-pmxxzUIASL9V25Hk](https://pubs.geoscienceworld.org/msa/ammin/article/77/11-12/1166/42628/Kinetics-of-the-marcasitepyrite-transformation-An?casa_token=j8FzrxhbbcAAAA: DydykzhVazgSGF8zLkUd_NYcOLy6w0qLEZNMsoCUGzQRIO_wzMJq_7g-pmxxzUIASL9V25Hk)

40. Blount AM Nature of the alterations which form on pyrite and marcasite during collection storage. In: Collection Forum; 1993. pp. 1–16.
41. Conn CD, Spry PG, Layton-Matthews D, Voinot A, Koenig A. The effects of amphibolite facies metamorphism on the trace element composition of pyrite and pyrrhotite in the Cambrian Nairne pyrite member, Kanmantoo Group, South Australia. *Ore Geol Rev.* 2019;114:103128. <https://doi.org/10.1016/j.oregeorev.2019.103128>

**How to cite this article:** Uwanyuze RS, Enright L, Zhang J, Schafföner S. Preparation of concrete specimen for internal sulfate attack analysis using electron backscatter diffraction. *Int J Appl Ceram Technol.* 2022;19:1195–1207.

<https://doi.org/10.1111/ijac.13973>